Sulfurized Polyacrylonitrile (SPAN): Changes in Mechanical Properties during Electrochemical Lithiation

Saul Perez Beltran[1], and Perla B. Balbuena[1,2,3],*

[1]Department of Chemical Engineering, [2]Department of Materials Science and Engineering, and [3]Department of Chemistry, Texas A&M University, College Station, Texas 77843, United States

*e-mail: balbuena@tamu.edu

Abstract

Sulfurized polyacrylonitrile (SPAN) is a promising material for stable lithium-sulfur (Li-S) batteries that can potentially satisfy the demand for high-density energy storage devices for electric vehicles (EVs). However, important physical and chemical properties of the SPAN cathode material are not yet well understood. For example, the SPAN mechanical behavior that depends on the structure and chemistry of the material generated during synthesis, and the mechanical response evolution during battery discharge have been scarcely investigated. This work addresses the effects of electrochemical lithiation on the SPAN mechanical integrity via uniaxial tensile loading tests using molecular dynamics with the ReaxFF potential. We evaluate the volume expansion, Young's modulus, yield strength, and ultimate tensile strength with increasing lithium contents. Our results show how the degree of graphitization of the carbonized skeleton impacts the SPAN ability to withstand the volume expansion-induced structural stresses upon lithiation. We describe the fracture mechanisms and find out a ductility loss with increasing lithium contents.

Introduction

The sulfurized polyacrylonitrile (SPAN) is a low-cost composite material that constitutes itself as a game-changer for lithium-sulfur (Li-S) batteries, one of the most promising electrochemical systems to replace current Li-ion batteries in high-energy density applications.[1-4] The SPAN material enhances the low sulfur electronic conductivity, suppresses lithium-polysulfides (Li-PSs) dissolution during cycling, and has the potential to deliver specific energy close to ~1176 W h kg^{-1} assuming complete reaction to Li_2S.[5-7] The SPAN material differentiates from other sulfur-carbon composites because of the covalent C-S bonding produced after high-temperature PAN pyrolyzation with sulfur.[8-10] The covalent interaction between sulfur and the graphitized carbon skeleton changes the sulfur aggregation from its typical eight-membered crown ring

orthorhombic configuration to a short-length sulfur chains distribution (-S_x- x ≤ 4). The SPAN material's complex structural features induce a single-plateau and slightly sloped voltage discharge profile centered at 1.7 V vs. Li/Li^+,[9, 11] deviated from the typical two-sloped discharge profile found in elemental sulfur.[12] Details on the SPAN electrochemical lithiation mechanism and its compatibility with ether and carbonate-based electrolytes are available in earlier publications on this topic from our work and that from other authors.[6, 11, 13-14]

Regardless of the high interest in the SPAN electrochemical behavior,[6] there are only few reports on the material's mechanical response with lithiation. One experimental study indicates a 22% cathode volume expansion in a Li-S battery with SPAN 40 wt. % sulfur loading mixed with acetylene black and polytetrafluoroethylene (PTFE) to an 80:15:5 weight ratio discharged down to 1.0 V vs. Li/Li^+.[15] Moreover, our DFT calculations indicate a 45.4% expansion for a SPAN model (42 wt. % sulfur) after discharge to 1.0 V vs. Li/Li^+,[13] significantly lower than the ~ 80 % increase for elemental sulfur after reduction to Li_2S.[16-17] However, no other experimental or theoretical work provides information specific to the SPAN volume expansion in the over-discharge regime (0 V vs. Li/Li^+) or the structural SPAN integrity upon discharge. Not even after multiple works point out to a SPAN stable cyclability and high capacity if operated between 0.1 and 3.0 V vs. Li/Li^+.[18]

This work addresses the effects of lithiation on the SPAN mechanical integrity via uniaxial tensile loading tests using classical molecular dynamics simulations with the ReaxFF potential. Our goal is to provide information on the SPAN's response during discharge, potentially influencing its ability to interact with binders and current collectors in complex cathode architectures. The ReaxFF potential is particularly well suited for modeling fracture because of its ability to treat covalent bond cleavage events that evolve into local stress concentrations and crack growth.[19] We first create a representative model for lithiated SPAN following a sequential simulation protocol that emulates a sequential synthesis procedure where the PAN carbonization precedes the sulfurization and subsequent lithiation.[4, 8] We measure the main structural features before lithiation in terms of the skeleton's graphitization degree and sulfur aggregation state. We proceed to evaluate the volume expansion, Young's modulus (YM), yield strength, and ultimate tensile strength (UTS) with increasing lithium contents.

Our results highlight the skeleton graphitization's impact on the SPAN mechanical properties, mainly on the material's response to deformation throughout the electrochemical lithiation, which motivates the design of new synthesis protocols able to produce SPAN composites with both high graphitization degrees and high sulfur loading. [6, 20] The fracture analysis shows that

the carbon skeleton aligns its graphitized domains along the strain direction to withstand the external tensile force. However, lithiation still makes the material to lose ductility, and the induced volume expansion reduces the material's response to further deformation. These results provide design guiding information to improve the SPAN mechanical response to discharge, and the reported data is useful for development of continuum models to elucidate morphological changes and failure mechanisms in length and time scales comparable with experiments.[21]

Computational and Simulation Methods

ReaxFF Parameterization

We perform our molecular dynamics (MD) simulations using the ReaxFF force field style (reax/c) implemented in the Large-scale atomic/molecular massively parallel simulation package (LAMMPS, version 3 Mar 2020).[22] The ReaxFF force field suits well for modeling chemically reactive systems as it uses a bond-order/bond-distance relation, coupled with a bond-order/bond-energy relation, to address bond-formation/bond-breaking events.[23] Representative examples of ReaxFF use are combustion simulations, fuel cell polymers, battery materials, polymer cross-linking, and Kevlar mechanical properties.[24] For the case of evaluating mechanical properties, the ReaxFF performs particularly well for modeling fracture because of its ability to treat covalent bond cleavage.[19]

The ReaxFF parameterization used for this work is the one developed for carbonization processes of C/H/O/H-based polymers (C/H/O/H-2019),[25] combined with the ReaxFF parameterization used in an earlier study on the influence of Teflon on the tetra-(ethylene glycol) dimethyl ether (TEGDME) decomposition on LiS batteries.[26] These two parameterizations merged are within the same development ReaxFF branch and proved adequate in earlier works focused on PAN carbonization and sulfur lithiation processes.[17, 24-27] The C/H/O/H-2019 parameterization provides an adequate estimation of graphene mechanical properties and is suitable for modeling small byproduct molecules' production during carbonization processes, such as CO_2, CO, H_2O, H_2, and N_2, with a particular focus on N_2 formation kinetics. The second parameterization addresses the lithium/sulfur interactions with carbon, nitrogen, and hydrogen. The ReaxFF force field enjoys high intra-transferability and the two parameterizations merged provided all pair and angle interactions between the atomic species present in our simulations.[24]

SPAN Synthesis and Lithiation Simulation Protocols

We perform our calculations on a SPAN structure representing a SPAN nanoparticle without direct interaction with the electrolyte. This assumption is valid based on the small pore size distribution of sulfurized carbon composites and the formation of a solid electrolyte interphase (SEI) coating on the composite's surface with carbonate-based electrolytes.[6, 33-34]

We follow a three-step simulation protocol to build the lithiated SPAN structures. First, we create a carbonized PAN (c-PAN) structure, followed by a sulfurization procedure to obtain the SPAN structure, and finally, we model the SPAN lithiation (Li-SPAN). This simulation procedure for the SPAN synthesis emulates a two-step SPAN synthesis procedure similar to experiments where the PAN dehydrogenation precedes the sulfurization process.[4, 8]

For the carbonization step, Figure 1 shows 48 idealized ladder PAN structures with four repetitive units each, packed randomly to a 1.6 g/cm^3 density[28] within a cubic simulation cell (30 Å x 20 Å x 20 Å) with periodic boundary conditions along the x-, y-, and z-coordinates. Earlier carbon fiber's carbonization simulations with PAN/graphene show that the polymer chains' initial alignment affects neither the all-carbon ring formation dynamics nor the gas byproduct production.[27]

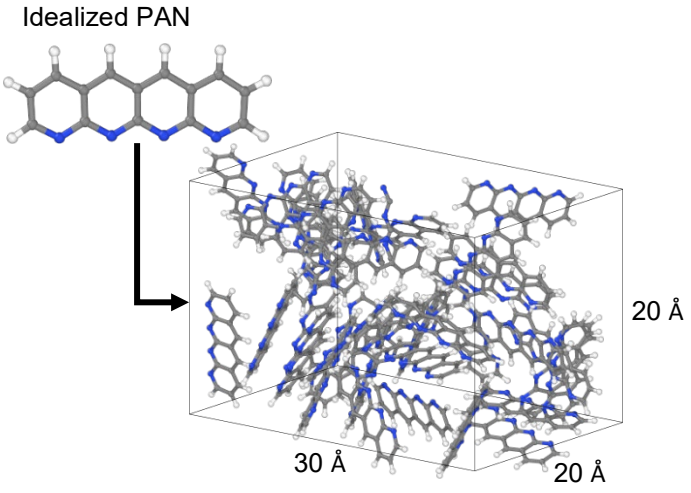

Figure 1: Simulation cell configuration before carbonization at 2500 K.

The carbonization simulation proceeds at 2500 K after a 33 K/ps linear ramp heating, with H_2 and N_2 molecules (produced due to PAN cyclization) removed every 65 ps. The heating stage uses an NVT ensemble and the Nose-Hoover thermostat with the damping parameter set to 25 fs. For this simulation segment at 2500 K, we use the NpT ensemble (Nose-Hoover barostat with the pressure damping parameter set to 250 fs), adjusting the input pressure every 10 ps to

keep the density close to the PAN's approximate density of 1.6 g/cm^3.[28] We use a 0.25 fs time step across all simulations; earlier studies with the ReaxFF conclude that using a shorter than 0.5 fs time step allows a physically realistic prediction of the material mechanical response.[19]

The relatively higher than experiment temperature (2500 K) acts only as an accelerating tool that enables a significant amount of reactions within the nanosecond scale accessible for the atomistic MD simulations.[27] After 520 ps at 2500 K, we extract up to seven cell configurations every 420 ps and cool them down back to 300 K following a 33 K/ps cooling ramp, after which we obtain multiple c-PAN structures with varying degrees of carbonization. This cooling stage uses an NVT ensemble as in the initial heating stage.

The sulfurization proceeds for each c-PAN sample, for which we use the NpT ensemble set to 300 K and 1 atmosphere, with the insertion of a sulfur atom into the simulation cell every five ps. Sulfur insertion goes such that the added atom locates randomly within the simulation cell no closer than 1.9 Å to the closest neighbor atom. This procedure goes until reaching a 42 wt. % sulfur loading. A 42 wt. % SPAN sulfur content is close to the highest reported value from experiments to show stable cycling capacity and keep up to 97 % retention after almost one hundred cycles.[8, 29-30]

The SPAN structures' lithiation proceeds similarly to the preceding sulfurization step but with lithium atoms' insertion until the system reaches a ~2.9 Li/S molar ratio. Multiple experimental and theoretical works conclude that SPAN lithiation proceeds beyond the theoretical 2.0 Li/S molar ratio for lithiation of elemental sulfur.[8-9, 13, 31] Inserting lithium as a neutral atom keeps the unit cell neutral and accounts for the lithium-ion coming from the anode and the electron coming from the external circuit. The ReaxFF method uses the electronegativity equalization method (EEM) to equilibrate charges every time step of the simulation automatically.[24, 32]

Mechanical Properties

The calculation of the stress-strain relationship under uniaxial tensile loadings helps to evaluate the material's mechanical response. These simulations run with the NpT ensemble set to 330 K and zero atmospheres with the deformation applied along the x-coordinate at a constant engineering strain-rate. We use different strain-rates (1x10^9, 3x10^9, 1x10^{10}, 3x10^{10}, 1x10^{11}, 3x10^{11}, and 1x10^{12} s^{-1}) to assess the strain-rate's impact on the material's mechanical response.

Eq. 1 represents the p_{xx} element of the pressure tensor, and it allows the tensile stress calculation along the x-coordinate. The first term on the right uses components of the kinetic

energy tensor, and the second uses components of the virial tensor.[33] N is the number of atoms in the system, V is the system volume, and v_{kx}, r_{kx}, f_{kx} represent the x-components of the velocity, position, and force vectors for the k[th] atom. The N' term refers to periodic image (ghost) particles outside the central box, needed due to the use of periodic boundary conditions.

$$p_{xx} = \frac{\sum_k^N m_k v_{kx} v_{kx}}{V} + \frac{\sum_k^{N'} r_{kx} f_{kx}}{V} \quad \text{Eq. 1}$$

The YM modulus calculation is carried out via linear regression of the initial linear portion of the stress-strain curve. The yield strength computation is performed with the offset yield method;[34] the intersection between the stress-strain profile and a line parallel to the linear part of the stress-strain profile at 0.2 % strain offset. Finally, the UTS coefficient is defined as the maximum stress from the stress-strain curve.

Results and Discussion

PAN Carbonization (c-PAN)

Figure 2 (a) shows the PAN's carbonization temperature profile. After 520 ps at 2500 K, we take up to seven samples every 420 ps and cool them down back to 300 K. This procedure creates multiple carbonized PAN (c-PAN) models labeled in alphabetical order from A to G. Figure 2 (b) and (c) shows the configurations for models A and G at 300 K.

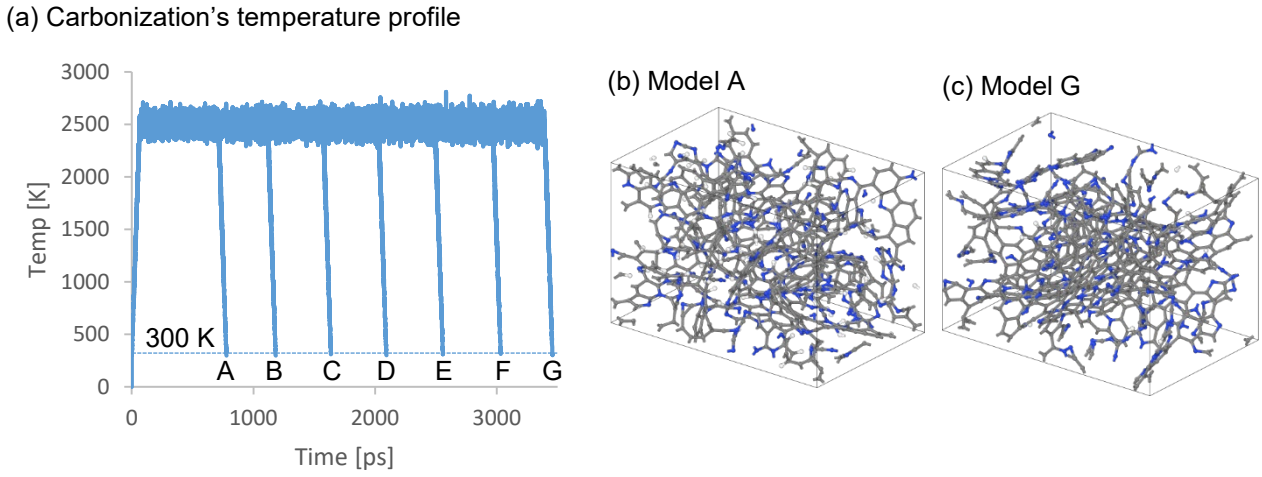

Figure 2: (a) PAN's carbonization temperature, (b) Model A, (c) Model G

The carbonization process transforms the initial PAN repetitive units into clusters acting as nucleation sites that form a defective graphitized structure. The partial radial distribution function (PRDF) profiles, averaged over 25 ps at 300 K, for models A and G in Figure 3 evidence the

formation of this graphitized structure. The first peak (~1.42 Å) corresponds to the C-C bond distance, the second one (~2.52 Å) reflects the distance between nearest neighbors in the same ring, whereas the third peak (~3.77 Å) is associated with atom pairs from adjacent carbon rings. Similarly, the fourth peak centered at ~4.25 Å represents long-range ordering between parallel graphene layers.[35-36] The second, third, and fourth peaks for model G's PRDF profile are more pronounced and slightly sharper than model A. As discussed later, this behavior corresponds to a higher graphitization degree due to longer carbonization at 2500 K (Fig. 2a). A visual inspection of Model G in Figure S1 highlights the long-range ordering between adjacent graphene-like layers, indicating that the structure effectively reaches the earlier formation stages of an extended three-dimensional graphitized structure. Figure S2 plots the PRDF profiles for interactions N-C, C-H, and N-H interactions for models A and G.

It is essential to point out that the structures derived from our carbonization simulations represent only the initial stages of a complete carbonization process. A fully graphitized model equivalent to a fully carbonized fiber material (CF) requires longer simulation times and bigger systems beyond the atomistic-scale.[21] However, our calculations provide new insights into the impact of lithiation processes' on the SPAN's mechanical response.

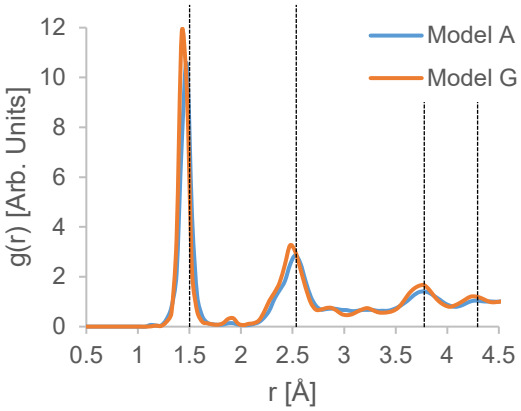

Figure 3: Partial radial distribution function (PRDF) profiles for the carbon-carbon interactions for models A and G.

The ratio of the in-graphene and peripheral carbons works as a proxy for quantifying the degree of graphitization.[27] The quantification of the degree of graphitization is essential because as shown later, it correlates to the SPAN's mechanical response upon lithiation, and it depends on the time that the system in the simulation cell spends at 2500 K before cooling down. The label in-graphene carbon corresponds to a carbon atom with three carbon neighbors (sp^2 carbon) belonging to a ring network (3- to 8-membered rings). On the other side, a peripheral carbon connects to one or two carbon neighbors, corresponding to the graphene sheet edges. Figure 4

(a) summarizes these two definitions; the gray-colored atoms correspond to in-graphene carbon while the red ones to peripheral carbon. Figure 4 (b) shows that the percentage of in-graphene carbon atoms (left vertical axis) increases from ~79 % to ~90 % from models A to B. Similarly, the peripheral carbon atoms decrease from ~21 % to ~10 % (right vertical axis); this behavior evidences that more extended carbonization simulation times effectively lead to a higher graphitization.

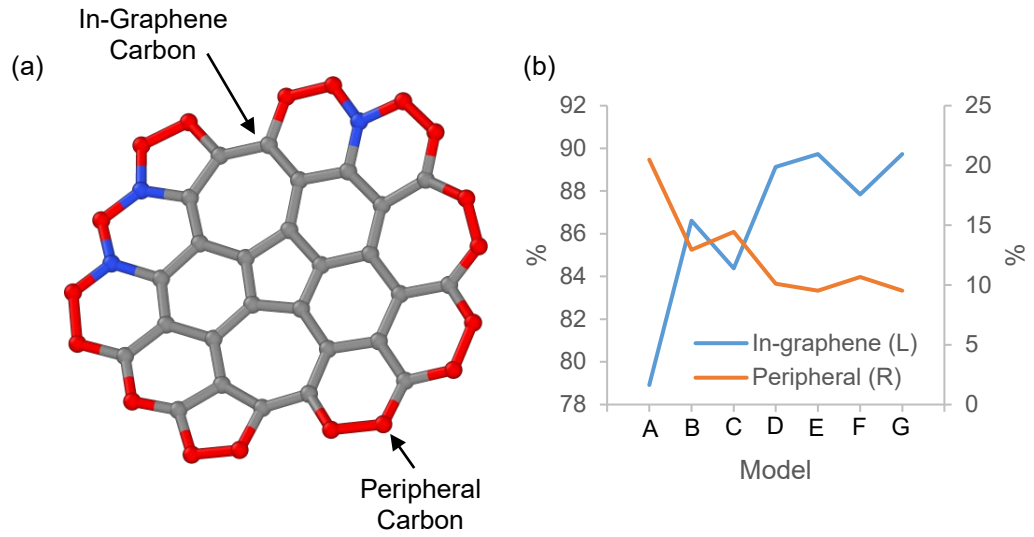

Figure 4: (a) The schematic of in-graphene carbons (gray spheres) and peripheral carbons (red spheres). Blue spheres are nitrogen atoms. (b) Percentage of in-graphene carbon atoms (left axis) and peripheral (right axis)

c-PAN Sulfurization (SPAN)

Figure 5 shows models A and G after sulfurization (42 wt. %S). The PRDF profiles for C-S and S-S interactions in Figure S3 indicate C-S bonding at 1.87 Å. The S-S peaks centered at ~2.32 Å (bonding S-S interactions) and ~3.52 Å (distance between second nearest sulfur neighbors in the same chain) suggest sulfur chains formation within the structure. Figure 6 (a) plots the sulfur chain length distribution vs. sulfur loading for model G. Below a ~23 wt % sulfur loading, two-membered sulfur chains dominate. However, this trend shifts toward three-membered sulfur chains for higher sulfur loadings. Figure 6 (b) shows that three-membered sulfur chains dominate across all models after reaching a ~42 wt % sulfur loading, regardless of changes in the graphitization degree. Both the PRDF profiles and the sulfur-chain distribution plots agree with X-ray photoelectron spectroscopy (XPS) measurements that suggest that in SPAN materials, sulfur is in the form of short-sulfur chains covalently bonded via either end to the carbonized backbone.[31, 37]

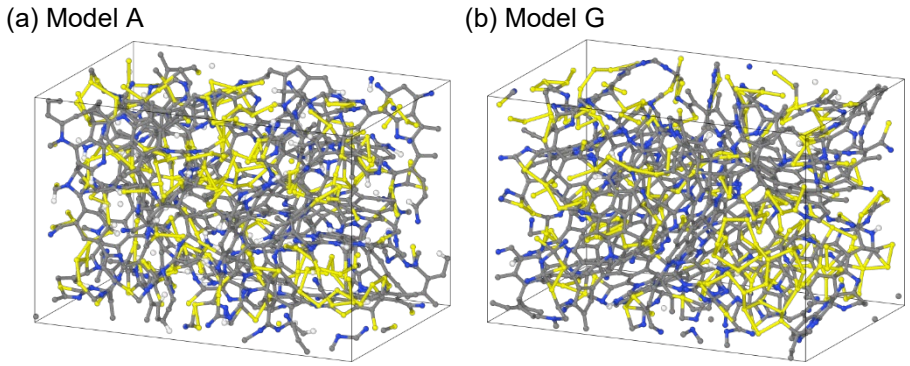

Figure 5: SPAN: (a) sulfurized model A (42 wt. % sulfur), (b) sulfurized Model G (42 wt. % sulfur).

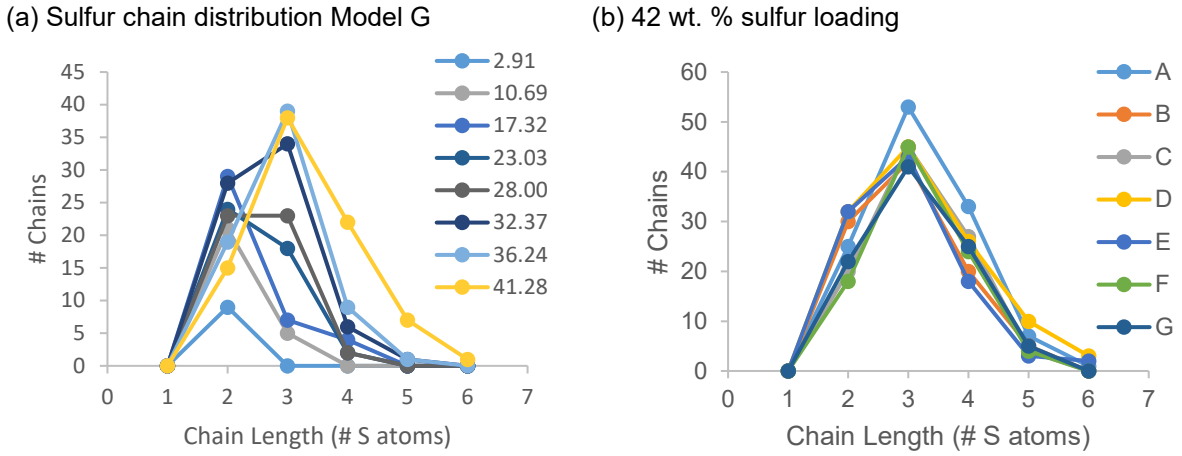

Figure 6: (a) Sulfur chain distribution vs. sulfur loading for model G, (b) sulfur chain distribution for a 42 wt % sulfur loading across all SPAN models.

SPAN Lithiation (Li-SPAN)

Figure 7 (a) corresponds to model A lithiated to a 2.90 Li/S molar ratio and it shows that the sulfur reduction products grow in the carbonized structure's in-between space. On the other side, Figure 7 (b) plots the total volume and density changes with the increasing lithium content. For a 2.0 Li/S ratio, the volume change is close to 56 %, and the density reduces from 2.26 g/cm^3 (before lithiation) to 1.67 g/cm^3. These results are in qualitative agreement with earlier DFT calculations on the SPAN lithiation that indicate a 45.4 % volume change after a lithiation close to a 2.0 Li/S molar ratio, equivalent to a discharge down to 1.0 vs. Li/Li$^+$.[13] Cathode's volume change measurements performed on a SPAN-based Li-S battery with a 32 wt. % sulfur loading also shows qualitative agreement with our results at they indicate a 22 % volume increase after discharge to 1.0 V vs. Li/Li$^+$.[15] Regarding the density's change, the 1.67 g/cm^3 density is in close agreement with the reported for Li_2S (1.66 g/cm^3).[24, 38] The density plot also shows no significant density changes with further lithium loading (above 2.0 Li/S molar ratio),

dropping only to 1.6 g/cm^3 after reaching a 2.9 Li/S molar ratio. This behavior indicates that sulfur reduction completes after achieving a 2.0 Li/S molar ratio, in agreement with our earlier DFT calculations for the SPAN material.[13] The PRDF profile for the S-S interactions and the sulfur-chain distribution plots vs. the Li/S ratio in Figure 8 (a) and (b) complement this affirmation. The S-S bond interactions (~2.2 Å) disappear almost entirely after a 2.0 Li/S molar ratio, whereas the sulfur-chain distribution shows no larger than two-membered sulfur chains with lithium loadings as low as 0.4 Li/S molar ratio. For higher Li/S molar ratios, only one-membered sulfur chains dominate. One-membered sulfur chains refer to those sulfur atoms engaged in C-S bonding interactions with no pendant S-S bonding interactions. Figure S4 summarizes the PRDF profiles for the S-S, S-Li, and C-Li interactions, and the sulfur-chain distribution plots for Model G; we observe a lithiation behavior similar to model A. Moreover, the C-Li profile suggests the C-Li bonding interactions become increasingly important with a 2.0 and above Li/S molar ratio, in agreement with our earlier DFT-based observations on the SPAN lithiation mechanism that highlight the carbonized skeleton's electrochemical active role at lower than 1.0 V vs. Li/Li$^+$ discharge voltages.[13]

(a) Model A – Li/S = 2.9

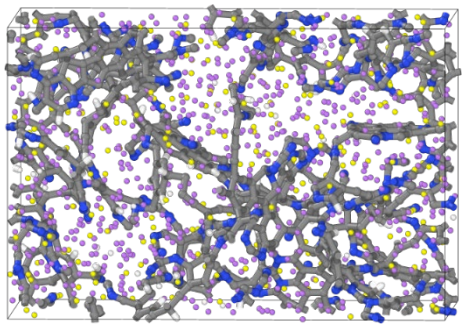

(b) Model A – Lithiation Behavior

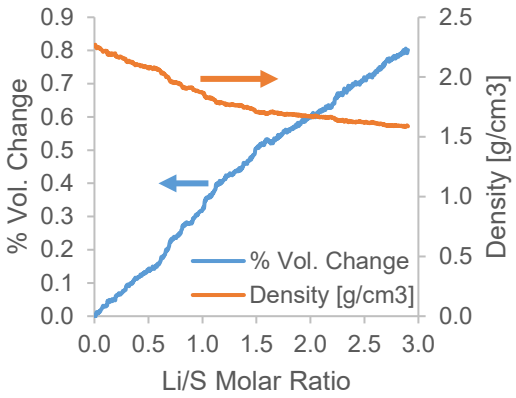

Figure 7: (a) Lithiated Model A (2.9 Li/S molar ratio, (b) Model A - structural response upon lithiation. Carbon atoms are the grey spheres, nitrogen atoms the blue ones, hydrogen is in white, sulfur in yellow, and lithium is purple.

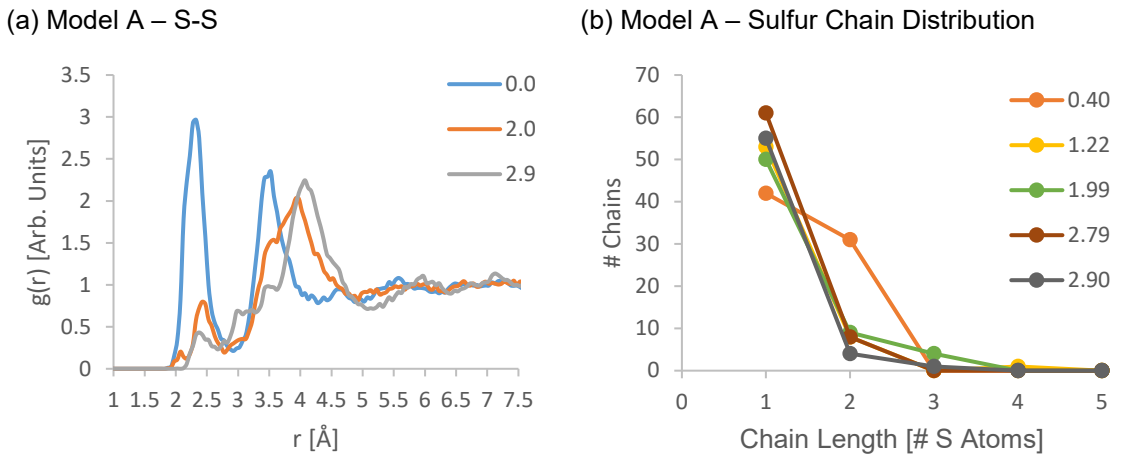

Figure 8: (a) PRDF function for the S-S interactions in sulfurized model A for three different Li/S molar ratios, (b) sulfur chain distribution in sulfurized model A with increasing Li/S molar ratios.

Mechanical Properties

c-PAN Response

Figure 9 (a) shows the effect of three different strain-rates ($1x10^{9}$, $3x10^{10}$, and $1x10^{12}$ s^{-1}) on the stress-strain measurements performed on Model A before sulfur loading. The two lower strain-rates show a saw-like strain-stress profile past the elastic limit that disappears for the faster loading at $1x10^{12}$ s^{-1}. Figure S5 shows the stress-strain curves with the entire strain-rates range proposed in the computational and simulation methods section. Amorphous Ni-nanowire materials and lithiated sulfur cathode structures show this same frequency-dependent behavior.[17, 39] Figure 9 (b) shows the YM modulus and the UTS coefficient calculated from the stress-strain measurements performed on Model A with multiple strain-rates. Both the YM and the UTS measurements are frequency-dependent, a behavior also observed in stress-strain experiments for amorphous materials.[40] The frequency-dependence increases with higher strain-rates (the YM modulus measured at $1x10^{12}$ s^{-1} is 1.7 times higher than the one calculated with a $1x10^{11}$ s^{-1}), but it also shows better convergence with strain-rates lower than $3x10^{10}$ s^{-1}. We choose the strain-rate $1x10^{10}$ s^{-1} for our further calculations; the good convergence relative to lower strain-rates suggests that the system already reaches the equilibrium condition between two successive strain events for this strain-rate.[17] Figure S6 shows the same behavior for both the YM modulus and UTS coefficient for model G. Figure S7 shows the stress-strain curves, the YM modulus, the yield strength, and the UTS coefficients measured for three different models created following the same carbonization path for Model A and the same strain-rate of $1x10^{10}$ s^{-1}. Table S1 summarizes these measurements too. The relatively small standard

deviation in these properties for these three models indicate the significance of our measurements.

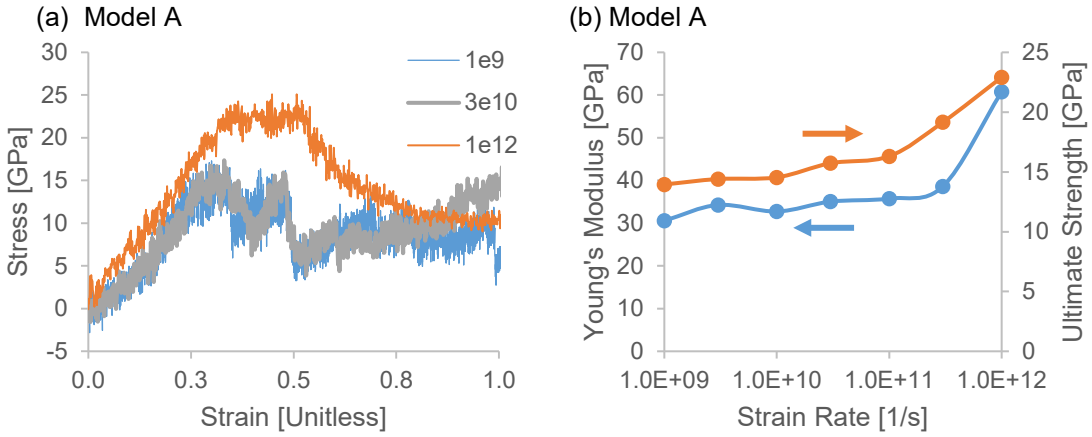

Figure 9: (a) Stress-strain curves for c-PAN (model A) with different strain-rates ($1x10^{9}$, $3x10^{10}$, and $1x10^{12}$ s^{-1}). (b) YM modulus and UTS coefficient Model A vs. strain deformation rate.

SPAN Response

Figure 10 shows the YM modulus calculated for all SPAN models (42 wt. % S loading). The YM magnitude does not significantly change after sulfur loading for each model, meaning that the carbonized skeleton dictates the material's mechanical response regardless of the sulfurization. Moreover, the trend shows an increase in YM modulus from model A to model G, in correlation with our earlier observation that longer carbonization times lead to higher graphitized structures; longer carbonization times yield more robust mechanical response to deformation. However, past the elastic limit, the carbonization time does not show significant influence on the yield strength (YS) and UTS coefficient, as both quantities do not display a clear trend from Model A to model G; the UTS coefficient increases to 12.6 GPa for model G, but this increase is only five GPa higher than in model A.

The YM modulus for carbonized PAN carbon fibers synthesized at 2300 K is 298 GPa, with the UTS coefficient equal to 3.11 GPa with a 1.53% strain to failure.[21] Our SPAN structures show a lower YM modulus and a higher UTS coefficient than carbonized carbon fibers across all models, which strongly suggests that our structures' carbonized backbone possess a lower graphitization degree than carbonized fibers. Moreover, the higher values than experiment UTS coefficients from our measurements are attributed to the much higher than experiments strain-rates and smaller samples used.[41] This behavior is most likely because elastic strain effects dominate with higher strain-rates, which enhances the flow stress directly affecting the

mechanical behavior.[41] On the other side, our relatively smaller than experiment samples also lead to divergences in the formation of concentration sites' mechanisms that might affect the dislocation nucleation mechanisms.[21, 42]

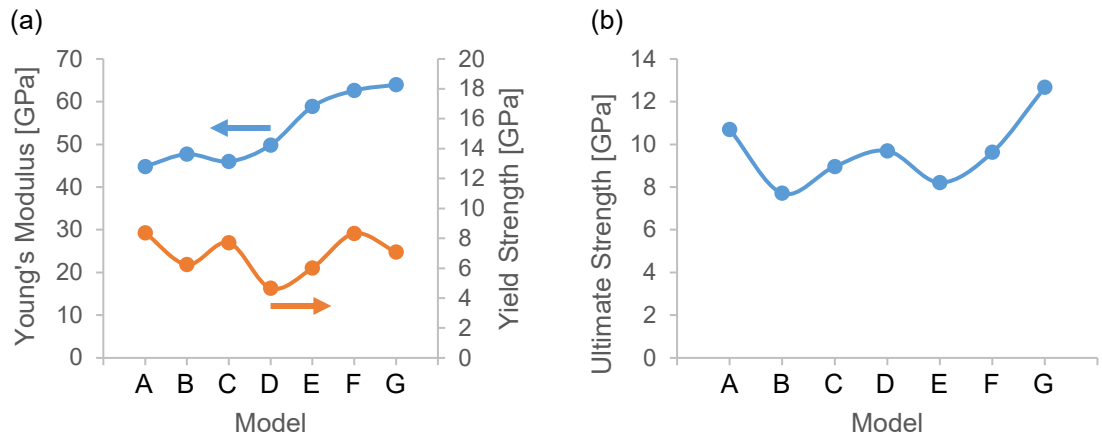

Figure 10: (a) YM modulus (left vertical axis) and Yield Strength (right vertical axis) from sulfurized models A to G (strain-rate 1x10^{10} s^{-1}). (b) UTS coefficient for sulfurized models A to G.

Li-SPAN Response

Figure 11 shows the YM modulus for models A and G as a function of the lithium loading. Model A shows an initial strengthening from 44.8 to 59.0 GPa, but it rapidly falls back to 43.4 GPa after a 0.8 Li/S molar ratio. Further lithium loading lowers the YM even more down to 35.2 GPa, and we observe no significant changes for 1.63 and above Li/S molar ratios. Model G shows a higher YM magnitude than model A regardless of the lithium content, and this is due to its higher graphitization degree, but it also displays a steady YM increment from 63.9 to 72.3 GPa until the Li/S molar ratio reaches 1.60, after which the YM monotonically lowers down to 49.4 GPa for a 2.73 Li/S molar ratio.

This YM's behavior vs. lithium loading correlates with the PRDF profiles for the S-S sulfur interactions and the sulfur-chain distribution plots for models A and G. The initial strengthening in Model A correlates with the PRDF profile plotted in Figure 8 (a) and the sulfur-chain distribution change in Figure 8 (b). The cleavage of S-S bonds opens the way for Li-S bond formation events that contribute to increased strength. However, higher lithiation does not lead to further changes in the sulfur-chain distribution; the sulfur reduction completes close to a 2.0 Li/S molar ratio, and changes in the material's mechanical response are less evident. For a 2.0 Li/S molar ratio and above, the calculated YM's magnitude (~36.4 GPa) is in close agreement

with the reported YM modulus for Li_2S (~35 GPa),[17, 43] which suggests that with high lithium loadings, the sulfur reduction products dominate the mechanical response of model A.

For model G, the high graphitization degree induces an initial sulfur-chain distribution centered on three-membered sulfur chains but with a relatively higher number of four and five-membered sulfur chains than in model A (Figure 6 (b)). Hence, the combined effect of S-S bonds cleavage and Li-S bond formation events persisting with higher lithium loadings contributes to a sustained YM increase up to a 1.6 Li/S molar ratio. However, further lithiation weakens the carbonized skeleton due to the volume expansion-induced structural stresses; hence, the sulfur reduction products increasingly dominate the material's mechanical response, such as the YM modulus converges to 49. 9 GPa.

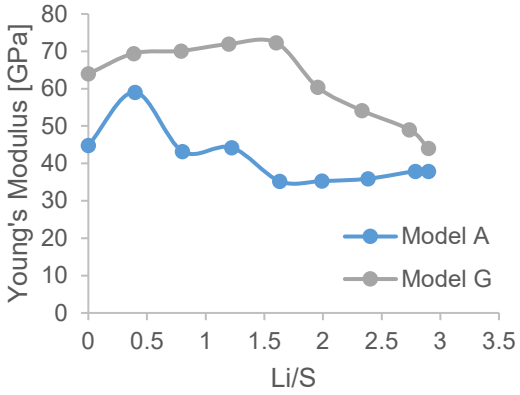

Figure 11: YM modulus for sulfurized models A and G vs. lithium content.

Figure 12 shows the yield strength and UTS coefficients for models A and G with increasing lithium contents. Both structures show the same decreasing trend for both coefficients as the lithium content increases. The monotonic lowering for both coefficients suggests that regardless of the backbone graphitization degree, the material ability to withstand further deformation decreases as the discharge proceeds; the material losses ductility. The growth of sulfur reduction products occupying the in-between empty spaces of the carbonized structure reduces the skeleton's ability to react to the external force.

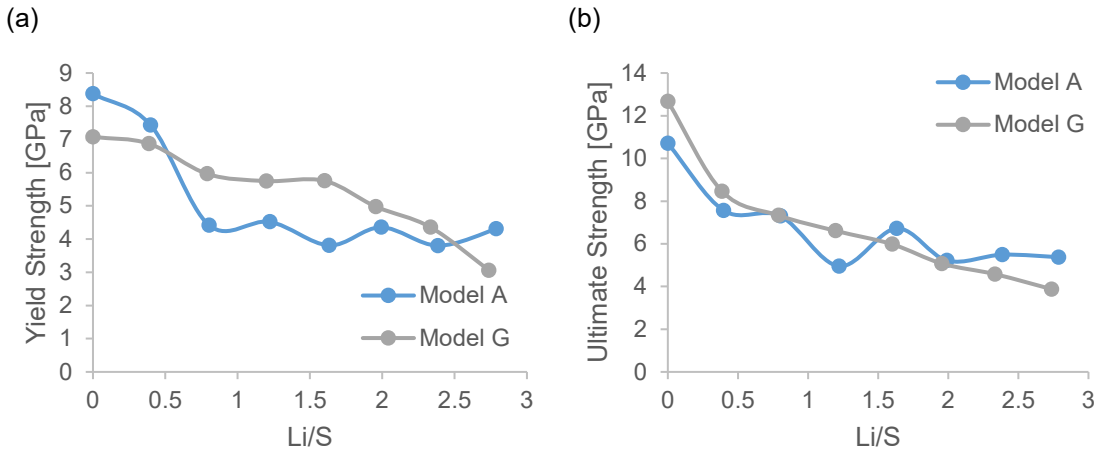

Figure 12: (a) Yield strength and (b) UTS coefficients for models A and G (42 wt. % sulfur loading) vs. lithium content.

Fracture Mechanism

Figure 13 (a) and (b) shows selected frames for model G under uniaxial strain before and after a 2.0 Li/S molar ratio. Before lithiation, the applied tension creates multiple small voids in the structure, and further deformation increases the number of these small voids that soon start nucleating. This coalescence reduces the cross-sectional area (necking) to eventually lead to the material's rupture after a strain close to 99%. The S-S bonds break in the earlier deformation stages, such as the initial voids in the structure growing where sulfur concentration is higher. Simultaneously, the carbonized backbone accommodates such as the defective graphene sheets partially align themselves along the strain direction; light-weighted three-dimensional (3D) graphene assemblies show similar alignment behavior.[44] However, further deformation leads to C-C and C-N breaking, triggering necking growth; eventually, the material's response to the deformation weakens, ultimately failing. The extended material deformation before failure comes from the carbonized backbone's ability to reorient the graphene sheets along the strain direction. This behavior shows that the carbonized skeleton modifies the sulfur's state of aggregation from the typical eight-membered crown rings to a short-length chain distribution and improves the mechanical response to external deformation. After reaching a 2.0 Li/S molar ratio, the material displays a similar reaction to deformation; the small voids grow via Li-S bond breaking in regions where the sulfur reduction products accumulate. However, the material fails soon after reaching a 50% strain, showing that lithiation reduces ductility. The stress-strain curves plotted in Figure 13 (c) for three different Li/S molar ratios confirm this behavior; fracture comes earlier with higher lithium contents. The SPAN's lithiation process

leads to a ~56 % volume expansion for a 2.0 Li/S molar ratio; volume expansion reduces the material's mechanical response to further deformation.

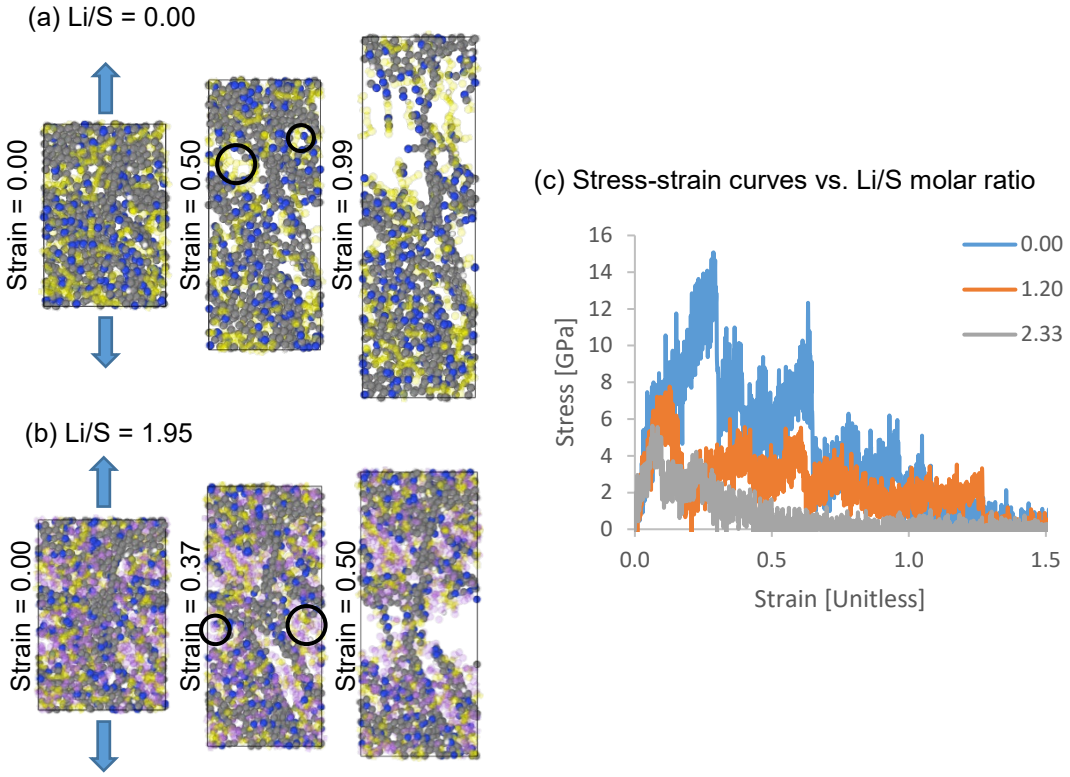

Figure 13: Fracture behavior in Model G (a) before lithiation and (b) after lithiation to a 1.95 Li/S molar ratio, (c) stress-strain curves for three different Li/S molar ratios.

Conclusions

Our calculations successfully address the SPAN mechanic response's evolution during discharge for varying degrees of the carbonized backbone graphitization. A higher graphitization level leads to a more robust mechanical response without significant impact on the sulfur-chain length distribution. This finding opens the way to search for SPAN synthesis procedures with high graphitization degrees and high sulfur loadings (~42 wt. %). The SPAN lithiation process leads to a volume expansion that barely changes with a higher graphitization degree. However, the mechanical response to deformation improves with a higher graphitization degree; the YM modulus increases overall, and the material strength improves into a broader interval of lithium contents. However, the increase in lithium content still makes the material brittle, and we observe a significant reduction in ductility throughout the lithiation process. These calculations provide input information for continuum modeling to address morphological changes and fracture dynamics in length and time scales comparable with experiments.

Supporting Information

The following information is available: Carbonized PAN structure (Model G) formed upon PAN cyclization (Fig. S1), PRDFs for models A and G before (Fig. S2) and after sulfurization (Fig. S3), PRDFs and S-chain length distribution in sulfurized model G during lithiation (Fig. S4), Stress-strain curves for c-PAN (model A) under a wide range of strain-rates (Fig. S5), Young Modulus and Ultimate Strength as function of strain rates for model G (Fig. S6), Evaluation of standard deviations in equivalent models A (Fig S7), Mechanical response for three equivalent models A before sulfurization (Table S1).

Acknowledgements

This material is based upon work supported by the U.S. Department of Energy's Office of Energy Efficiency and Renewable Energy (EERE), as part of the Battery 500 Consortium, Award Number DE-EE0008210. Supercomputer resources from the Texas A&M University High Performance Computer Center and Texas Advanced Computing Center (TACC) are gratefully acknowledged.

References

1. Barghamadi, M.; Kapoor, A.; Wen, C., A Review on Li-S Batteries as a High Efficiency Rechargeable Lithium Battery. *J. Electrochem. Soc.* **2013,** *160* (8), A1256-A1263.
2. Chung, S.-H.; Chang, C.-H.; Manthiram, A., Progress on the Critical Parameters for Lithium–Sulfur Batteries to be Practically Viable. *Adv. Funct. Mater.* **2018,** *28* (28), 1801188.
3. Yang, Y.; Zheng, G.; Cui, Y., Nanostructured Sulfur Cathodes. *Chem Soc Rev* **2013,** *42* (7), 3018-3032.
4. Li, H.; Xue, W.; Xu, W.; Wang, L.; Liu, T., Controllable Synthesis of Sulfurized Polyacrylonitrile Nanofibers for High Performance Lithium–Sulfur Batteries. *CompComm* **2021,** *24*, 100675.
5. Chen, W.-J.; Li, B.-Q.; Zhao, C.-X.; Zhao, M.; Yuan, T.-Q.; Sun, R.-C.; Huang, J.-Q.; Zhang, Q., Electrolyte Regulation towards Stable Lithium-Metal Anodes in Lithium–Sulfur Batteries with Sulfurized Polyacrylonitrile Cathodes. *Angew. Chem., Int. Ed.* **2020,** *59* (27), 10732-10745.
6. Yang, H.; Chen, J.; Yang, J.; Wang, J., Prospect of Sulfurized Pyrolyzed Poly(acrylonitrile) (S@pPAN) Cathode Materials for Rechargeable Lithium Batteries. *Angew. Chem., Int. Ed.* **2020,** *59* (19), 7306-7318.
7. Doan, T. N. L.; Ghaznavi, M.; Zhao, Y.; Zhang, Y.; Konarov, A.; Sadhu, M.; Tangirala, R.; Chen, P., Binding Mechanism of Sulfur and Dehydrogenated Polyacrylonitrile in Sulfur/Polymer Composite Cathode. *J. Power Sources* **2013,** *241*, 61-69.
8. Fanous, J.; Wegner, M.; Grimminger, J.; Andresen, Ä.; Buchmeiser, M. R., Structure-Related Electrochemistry of Sulfur-Poly(acrylonitrile) Composite Cathode Materials for Rechargeable Lithium Batteries. *Chem. Mater.* **2011,** *23* (22), 5024-5028.
9. Wei, S.; Ma, L.; Hendrickson, K. E.; Tu, Z.; Archer, L. A., Metal–Sulfur Battery Cathodes Based on PAN–Sulfur Composites. *J. Am. Chem. Soc.* **2015,** *137* (37), 12143-12152.

10. Wang, L.; He, X.; Sun, W.; Li, J.; Gao, J.; Tian, G.; Wang, J.; Fan, S., Organic Polymer Material with a Multi-Electron Process Redox Reaction: Towards Ultra-High Reversible Lithium Storage Capacity. *RSC Adv.* **2013,** *3* (10), 3227-3231.
11. Weret, M. A.; Jeffrey Kuo, C.-F.; Zeleke, T. S.; Beyene, T. T.; Tsai, M.-C.; Huang, C.-J.; Berhe, G. B.; Su, W.-N.; Hwang, B.-J., Mechanistic Understanding of the Sulfurized-Poly(Acrylonitrile) Cathode for Lithium-Sulfur Batteries. *Energy Storage Mater.* **2020,** *26*, 483-493.
12. Zheng, D.; Liu, D.; Harris, J. B.; Ding, T.; Si, J.; Andrew, S.; Qu, D.; Yang, X.-Q.; Qu, D., Investigation of the Li–S Battery Mechanism by Real-Time Monitoring of the Changes of Sulfur and Polysulfide Species during the Discharge and Charge. *ACS Appl. Mater.* **2017,** *9* (5), 4326-4332.
13. Perez Beltran, S.; Balbuena, P. B., Sulfurized Polyacrylonitrile for High-Performance Lithium–Sulfur Batteries: In-Depth Computational Approach Revealing Multiple Sulfur's Reduction Pathways and Hidden Li+ Storage Mechanisms for Extra Discharge Capacity. *ACS Appl. Mater.* **2021,** *13* (1), 491-502.
14. Perez Beltran, S.; Balbuena, P. B., A Solid Electrolyte Interphase to Protect the Sulfurized Polyacrylonitrile (SPAN) Composite for Li–S Batteries: Computational Approach Addressing the Electrolyte/SPAN Interfacial Reactivity. *J. Mater. Chem. A* **2021**.
15. He, X.; Ren, J.; Wang, L.; Pu, W.; Jiang, C.; Wan, C., Expansion and Shrinkage of the Sulfur Composite Electrode in Rechargeable Lithium Batteries. *J. Power Sources* **2009,** *190* (1), 154-156.
16. Zheng, G.; Yang, Y.; Cha, J. J.; Hong, S. S.; Cui, Y., Hollow Carbon Nanofiber-Encapsulated Sulfur Cathodes for High Specific Capacity Rechargeable Lithium Batteries. *Nano Lett.* **2011,** *11* (10), 4462-4467.
17. Islam, M. M.; Ostadhossein, A.; Borodin, O.; Yeates, A. T.; Tipton, W. W.; Hennig, R. G.; Kumar, N.; van Duin, A. C. T., ReaxFF Molecular Dynamics Simulations on Lithiated Sulfur Cathode Materials. *Phys. Chem. Chem. Phys.* **2015,** *17* (5), 3383-3393.
18. He, X.; Pu, W.; Ren, J.; Wang, L.; Wang, J.; Jiang, C.; Wan, C., Charge/Discharge Characteristics of Sulfur Composite Cathode Materials in Rechargeable Lithium Batteries. *Electrochim. Acta* **2007,** *52* (25), 7372-7376.
19. Jensen, B. D.; Wise, K. E.; Odegard, G. M., The Effect of Time Step, Thermostat, and Strain Rate on ReaxFF Simulations of Mechanical Failure in Diamond, Graphene, and Carbon Nanotube. *J. Comput. Chem.* **2015,** *36* (21), 1587-1596.
20. Fanous, J.; Wegner, M.; Grimminger, J.; Rolff, M.; Spera, M. B. M.; Tenzer, M.; Buchmeiser, M. R., Correlation of the Electrochemistry of Poly(acrylonitrile)–Sulfur Composite Cathodes with their Molecular Structure. *J. Mater. Chem.* **2012,** *22* (43), 23240-23245.
21. Zhu, J.; Gao, Z.; Kowalik, M.; Joshi, K.; Ashraf, C. M.; Arefev, M. I.; Schwab, Y.; Bumgardner, C.; Brown, K.; Burden, D. E.;et al.,, Unveiling Carbon Ring Structure Formation Mechanisms in Polyacrylonitrile-Derived Carbon Fibers. *ACS Appl. Mater.* **2019,** *11* (45), 42288-42297.
22. Plimpton, S., Fast Parallel Algorithms for Short-Range Molecular Dynamics. *J. Comput. Phys.* **1995,** *117* (1), 1-19.
23. Russo, M. F.; van Duin, A. C. T., Atomistic-Scale Simulations of Chemical Reactions: Bridging from Quantum Chemistry to Engineering. *Nucl. Instr. Meth. Phys. Res. B* **2011,** *269* (14), 1549-1554.
24. Senftle, T. P.; Hong, S.; Islam, M. M.; Kylasa, S. B.; Zheng, Y.; Shin, Y. K.; Junkermeier, C.; Engel-Herbert, R.; Janik, M. J.; Aktulga, H. M.; *et al.*, , The ReaxFF Reactive Force-Field: Development, Applications and Future Directions. *npj Comput. Mater.* **2016,** *2*, 15011.
25. Kowalik, M.; Ashraf, C.; Damirchi, B.; Akbarian, D.; Rajabpour, S.; van Duin, A. C. T., Atomistic Scale Analysis of the Carbonization Process for C/H/O/N-Based Polymers with the ReaxFF Reactive Force Field. *The Journal of Physical Chemistry B* **2019,** *123* (25), 5357-5367.

26. Islam, M. M.; Bryantsev, V. S.; van Duin, A. C. T., ReaxFF Reactive Force Field Simulations on the Influence of Teflon on Electrolyte Decomposition during Li/SWCNT Anode Discharge in Lithium-Sulfur Batteries. *J. Electrochem. Soc.* **2014,** *161* (8), E3009-E3014.
27. Rajabpour, S.; Mao, Q.; Gao, Z.; Khajeh Talkhoncheh, M.; Zhu, J.; Schwab, Y.; Kowalik, M.; Li, X.; van Duin, A. C. T., Low-Temperature Carbonization of Polyacrylonitrile/Graphene Carbon Fibers: A Combined ReaxFF Molecular Dynamics and Experimental Study. *Carbon* **2021,** *174*, 345-356.
28. Newell, J.; Rogers, D.; Edie, D.; Fain, C., Direct Carbonization of PBO Fiber. *Carbon* **1994,** *32* (4), 651-658.
29. Wang, L.; He, X.; Li, J.; Chen, M.; Gao, J.; Jiang, C., Charge/Discharge Characteristics of Sulfurized Polyacrylonitrile Composite with Different Sulfur Content in Carbonate Based Electrolyte for Lithium Batteries. *Electrochim. Acta* **2012,** *72*, 114-119.
30. Fanous, J.; Wegner, M.; Spera, M. B. M.; Buchmeiser, M. R., High Energy Density Poly(acrylonitrile)-Sulfur Composite-Based Lithium-Sulfur Batteries. *J. Electrochem. Soc.* **2013,** *160* (8), A1169-A1170.
31. Wang, X.; Qian, Y.; Wang, L.; Yang, H.; Li, H.; Zhao, Y.; Liu, T., Sulfurized Polyacrylonitrile Cathodes with High Compatibility in Both Ether and Carbonate Electrolytes for Ultrastable Lithium–Sulfur Batteries. *Adv. Funct. Mater.* **2019,** *29* (39), Article no. 1902929.
32. Mortier, W. J.; Ghosh, S. K.; Shankar, S., Electronegativity-Equalization Method for the Calculation of Atomic Charges in Molecules. *J. Am. Chem. Soc.* **1986,** *108* (15), 4315-4320.
33. Thompson, A. P.; Plimpton, S. J.; Mattson, W., General Formulation of Pressure and Stress Tensor for Arbitrary Many-Body Interaction Potentials Under Periodic Boundary Conditions. *The Journal of Chemical Physics* **2009,** *131* (15), 154107.
34. Ross, C.; Bird, J.; Little, A., *Mechanics of solids*. Routledge: 2016.
35. Wang, Y.-X.; Huang, L.; Sun, L.-C.; Xie, S.-Y.; Xu, G.-L.; Chen, S.-R.; Xu, Y.-F.; Li, J.-T.; Chou, S.-L.; Dou, S.-X., Facile Synthesis of a Interleaved Expanded Graphite-Embedded Sulphur Nanocomposite as Cathode of Li–S Batteries with Excellent Lithium Storage Performance. *J. Mater. Chem.* **2012,** *22* (11), 4744-4750.
36. Wen, Y.; He, K.; Zhu, Y.; Han, F.; Xu, Y.; Matsuda, I.; Ishii, Y.; Cumings, J.; Wang, C., Expanded Graphite as Superior Anode for Sodium-Ion Batteries. *Nat. Commun.* **2014,** *5*, 4033.
37. Jin, Z.-Q.; Liu, Y.-G.; Wang, W.-K.; Wang, A.-B.; Hu, B.-W.; Shen, M.; Gao, T.; Zhao, P.-C.; Yang, Y.-S., A New Insight Into the Lithium Storage Mechanism of Sulfurized Polyacrylonitrile with No Soluble Intermediates. *Energy Storage Mater.* **2018,** *14*, 272-278.
38. Fang, R.; Zhao, S.; Sun, Z.; Wang, D. W.; Cheng, H. M.; Li, F., More Reliable Lithium-Sulfur Batteries: Status, Solutions and Prospects. *Adv. Mater.* **2017,** *29* (48), 1606823.
39. Branício, P. S.; Rino, J.-P., Large Deformation and Amorphization of Ni Nanowires Under Uniaxial Strain: A Molecular Dynamics Study. *Phys. Rev. B* **2000,** *62* (24), 16950-16955.
40. Falk, M. L.; Langer, J. S., Deformation and Failure of Amorphous, Solidlike Materials. *Annual Review of Condensed Matter Physics* **2011,** *2* (1), 353-373.
41. Davis, J. R., *Tensile Testing, 2nd Edition*. ASM International: 2004.
42. Tschopp, M. A.; Spearot, D. E.; McDowell, D. L., Atomistic Simulations of Homogeneous Dislocation Nucleation in Single Crystal Copper. *Modell. Simul. Mater. Sci. Eng.* **2007,** *15* (7), 693-709.
43. Sakuda, A.; Hayashi, A.; Tatsumisago, M., Sulfide Solid Electrolyte with Favorable Mechanical Property for All-Solid-State Lithium Battery. *Sci. Rep.* **2013,** *3*, 2261.
44. Qin, Z.; Jung, G. S.; Kang, M. J.; Buehler, M. J., The Mechanics and Design of a Lightweight Three-Dimensional Graphene Assembly. *Science Advances* **2017,** *3* (1), e1601536.

Table of Contents Figure